Journal of Sound and Vibration 326 (2009) 852–869

Contents lists available at ScienceDirect

Journal of Sound and Vibration

journal homepage: www.elsevier.com/locate/jsvi

Development and validation of a three-dimensional ring-based structural tyre model

P. Kindt *, P. Sas, W. Desmet

K.U. Leuven, Department of Mechanical Engineering, Division PMA, Celestijnenlaan 300B, 3001 Leuven, Belgium

ARTICLE INFO

Article history:
Received 16 October 2008
Received in revised form
14 May 2009
Accepted 14 May 2009
Handling Editor: C.L. Morfey
Available online 13 June 2009

ABSTRACT

This paper presents a structural model for an unloaded tyre, based on a three-dimensional flexible ring on an elastic foundation. The ring represents the belt and the elastic foundation represents the tyre sidewall. The model is valid up to 300 Hz and includes a submodel of the wheel and the air cavity. This makes the model potentially suitable for the prediction of structure-borne interior noise. Unlike most ring models, which only consider in-plane modes, the presented model also predicts the modes that involve torsion of the belt in circumferential direction. The parameterization of the model, which does not require detailed knowledge of the tyre construction, is based on the main geometrical properties of the tyre and a limited modal test. Comparison between measured and calculated responses shows that the tyre–wheel model describes the dynamic behaviour with acceptable accuracy. Since the model is physical, it can be applied to describe other operational conditions such as loading and rotation.

1. Introduction

1.1. Road traffic noise

The steady increase of road traffic density over the past decades caused an increasing noise burden for most inhabitants of industrialized areas [1]. In the European Union, it has been estimated that approximately 80 million people are exposed to unacceptably high traffic noise levels [2]. In addition, this type of noise is by far the most pervasive of the many noise sources that affects people [3]. The two main vehicle exterior noise sources are drivetrain noise and tyre/road noise. Despite the complexity of the involved noise sources, significant reductions of the drivetrain noise have been achieved, encouraged by the progressive vehicle noise legislation which was introduced during the 1970s in Europe. However, no improvements in tyre/road noise can be observed over the last decades [4]. Furthermore, the tendency towards wider tyres and larger wheel diameters adversely affects the tyre/road noise. As a result, the tyre/road interaction is currently the most important source of vehicle noise for driving speeds above 40 km/h [5]. Nowadays, the NVH (noise, vibration and harshness) performance of a vehicle has become a distinctive marketing and design criterion for vehicle manufacturers. Especially on rough road surfaces, the tyre/road interaction contributes significantly to the perceived vehicle interior noise and vibration levels in certain frequency ranges [6].

Based on their nature, tyre/road noise generating and amplification phenomena are divided in two groups: vibrational and aerodynamical phenomena [5].

* Corresponding author. Tel.: +32 16 32 24 80; fax: +32 16 32 29 87.
E-mail addresses: Peter.Kindt@mech.kuleuven.be (P. Kindt), Paul.Sas@mech.kuleuven.be (P. Sas), Wim.Desmet@mech.kuleuven.be (W. Desmet).

0022-460X/$ - see front matter © 2009 Elsevier Ltd. All rights reserved.
doi:10.1016/j.jsv.2009.05.019

The vibrational phenomena consider the structural vibrations of the tyre which are caused by the interactions between tyre and road. Different types of structural waves can be identified [7,8]: bending, longitudinal and shear waves. The exterior sound radiation due to the structural vibrations is significant below 1500 Hz and is found to be mainly caused by bending vibrations [9]. At frequencies below 500 Hz the tyre shows a distinct modal behaviour; this means that structural waves at certain frequencies interfere constructively. The damping of the tyre rubber increases with increasing frequency; thus causing the structural waves to decay rapidly in amplitude away from the excitation area. At for instance 3200 Hz, the response level drops by approximately 40 dB by half-way around the belt [10]. Pinnington and Briscoe [8] showed that no modal behaviour around the belt appears above 500 Hz, which means that the belt can be approximated as an infinite beam in the circumferential direction. In addition to the directly radiated exterior noise from a vibrating tyre, tyre vibrations are also transmitted through the spindle and suspension towards the vehicle. These vibrations then cause noise radiation in the vehicle interior. Measurements show that the interior noise below 400 Hz correlates very well to the forces measured at the spindle [11]. Moreover, the structure borne noise contribution dominates the interior noise below 500 Hz [6,12]. Besides the structural resonances of the tyre structure, acoustic resonances appear in the air cavity. The first cavity resonance for an unloaded tyre appears in the frequency range between 200 and 250 Hz. Sakata et al. [11] revealed that the acoustic cavity resonance contributes significantly to the interior tyre/road noise.

The aerodynamical phenomena can be described in general as air displacement mechanisms. The interaction between tyre and road causes pressure variations in the surrounding air. Similar to the structural vibrations, certain amplification and reduction effects appear which either amplify or reduce the noise propagation. The frequency range for this air-borne exterior noise is typically from 500 up to 3000 Hz [5]. In this paper, the aerodynamical phenomena will not be considered.

1.2. Structural tyre models

The increasing awareness for tyre/road noise and the resulting tyre/road noise reduction targets have increased the need for more accurate simulation tools. Due to the complexity of the tyre structure and the various effects that contribute in the generation of noise, several specific tyre models have been developed. For instance, the numerical models used for the design of low noise tyres are in general less suited for the development of low noise road surfaces. Moreover, a further distinction has to be made between models that are used in full vehicle simulations to predict the interior noise and models that predict the noise radiation from the tyre towards the environment. A wide range of tyre models are available, ranging from physical to statistical models [13]. In this paragraph a short overview of the available physical structural tyre models is given. Analytical models have been used since a long time to describe the dynamic behaviour of tyres. Both ring and plate models appear in literature. Ring models are mainly used to describe the in-plane dynamics and are based on a flexible ring with an elastic foundation, representing the tyre sidewalls [14,15]. More complex ring models use a viscoelastic multi-layered ring and include the air cavity dynamics in the elastic foundation [16]. However, due to the considerable simplifications, ring models cannot describe cross-sectional bending modes which appear at frequencies above 300 Hz. Plate models neglect the curvature of the tyre, which is a valid assumption for higher frequencies (above 400 Hz). Additionally, the internal structure gains importance due to more localized deformations at higher frequencies [7,17,18]. The tread and sidewalls are modelled as a thin, flat orthotropic plate, with in-plane tension.

A large number of tyre models are based on finite element methods. Those models are most appropriate for low frequencies (below 400 Hz) where the number of elements is still acceptable. Certain models describe the tyre structure with all its components in detail, which leads to large computation times [19,20]. Recently, Brinkmeier et al. [21] developed a finite element model to simulate the dynamic behaviour of a stationary rolling tyre in ground contact by using an arbitrary Lagrange–Eulerian formulation. In order to reduce the model size, a more common approach is to introduce simplifications in the tyre model. For instance, the tyre cross-section can be approximated by a single layer of shell elements which can have a variable thickness [22,23]. A similar model was proposed by Lopez et al. [24] to extract the eigenfrequencies and eigenvectors of a loaded tyre. Subsequently, the obtained modal base is transformed to determine the response of the rotating tyre in a fixed (Eulerian) reference frame. An alternative modelling approach is to consider the tyre as a waveguide [25]. Wave solutions in such structures can be found by a method called the waveguide finite element method. This method uses a finite element approach on the cross-section of the waveguide to model the vibro-acoustic response as a set of linear coupled one-dimensional wave equations. In general, simplifications made in analytical or numerical tyre models reduce the computational effort; however, the models become less capable in predicting the influence of a small design change.

The structural finite element tyre model presented in this paper is based on a three-dimensional flexible ring on an elastic foundation. The ring represents the belt and the elastic foundation represents the tyre sidewall. The model is valid up to 300 Hz and includes a model of the wheel and the air cavity. This makes the model potentially suitable for the prediction of structure borne interior noise. Unlike most ring models which consider only in-plane motion, the presented model also predicts modes that involve torsion of the belt in circumferential direction. The parameterization is based on the main geometrical properties of the tyre and a limited modal test. The model in this paper is validated on a tyre (size 205/55R16) without tread pattern, which is mounted on a steel wheel.

Although the model only provides response of points on the treadband, it can also be used to predict the structure-borne noise radiation below 300 Hz. In this frequency range, the noise radiation is mainly dominated by the tread area [6].

Driving on roads with cobblestones, transverse joints, railroad crossings, etc. are situations in which the exterior tyre noise is dominated by structure-borne noise radiation below 500 Hz.

2. Analytical ring model

This chapter derives the equations of motion for a flexible ring on an elastic foundation. The dynamic behaviour of a tyre can be approximated by this system in which the flexible ring represents the belt and tread layer; the elastic foundation represents the tyre sidewall. The effect of the circumferential tension in the ring due to the internal pressure is taken into account in the equations of motion. Subsequently, an expression for the natural frequencies is derived. This expression will be used in Section 3 to calculate the tyre sidewall stiffness out of the measured tyre natural frequencies.

2.1. Equations of motion

Fig. 1 shows a drawing of the flexible ring on elastic foundation. The displacements u_3 and u_θ are the radial and tangential displacement of the neutral surface, respectively. The neutral surface is referred to as the surface where the stresses are of a membrane type; bending stresses are zero in the neutral surface. All displacements are considered to be constant over the belt width. The radius, thickness, width and density of the ring are R, h, b and ρ, respectively. The inner surface of the ring is subjected to a pressure p (Pa). k_3 and k_θ are the stiffness values per unit area (N m^{-3}) of the distributed radial and tangential linear springs. q_3 and q_θ are the distributed loads per unit area. The equations of motion for the ring are [14]

$$\frac{D}{R^4}\left(\frac{\partial^2 u_\theta}{\partial\theta^2}-\frac{\partial^3 u_3}{\partial\theta^3}\right)+\frac{K}{R^2}\left(\frac{\partial^2 u_\theta}{\partial\theta^2}+\frac{\partial u_3}{\partial\theta}\right)+\frac{N^r_{\theta\theta}}{R^2}\left(\frac{\partial u_3}{\partial\theta}-u_\theta\right)-k_\theta u_\theta-\frac{p}{R}\left(\frac{\partial u_3}{\partial\theta}-u_\theta\right)+q_\theta=\rho h\frac{\partial^2 u_\theta}{\partial t^2} \tag{1}$$

$$\frac{D}{R^4}\left(\frac{\partial^3 u_\theta}{\partial\theta^3}-\frac{\partial^4 u_3}{\partial\theta^4}\right)-\frac{K}{R^2}\left(\frac{\partial u_\theta}{\partial\theta}+u_3\right)+\frac{N^r_{\theta\theta}}{R^2}\left(\frac{\partial^2 u_3}{\partial\theta^2}-\frac{\partial u_\theta}{\partial\theta}\right)-k_3 u_3+\frac{p}{R}\left(\frac{\partial u_\theta}{\partial\theta}+u_3\right)+q_3=\rho h\frac{\partial^2 u_3}{\partial t^2} \tag{2}$$

D and K represent the bending and membrane stiffness, respectively. These stiffnesses are expressed as a function of Young's modulus E and the ring thickness h:

$$D=Eh^3/12 \tag{3}$$

$$K=Eh \tag{4}$$

The internal pressure on the ring causes a circumferential pretension in the ring. $N^r_{\theta\theta}$ represents the pretension force resultant in the ring per unit width of the ring (see Appendix A):

$$N^r_{\theta\theta}\approx\frac{pR}{1+k_3R^2/(hE)} \tag{5}$$

For the application considered in this paper, the circumferential pretension can be further approximated by pR.

Four assumptions were made to obtain the equations of motion (1) and (2). Firstly, transverse shear deflections ($\varepsilon_{\theta 3}$) of the ring are neglected. Secondly, all displacements are considered to be constant over the belt width (y-direction).

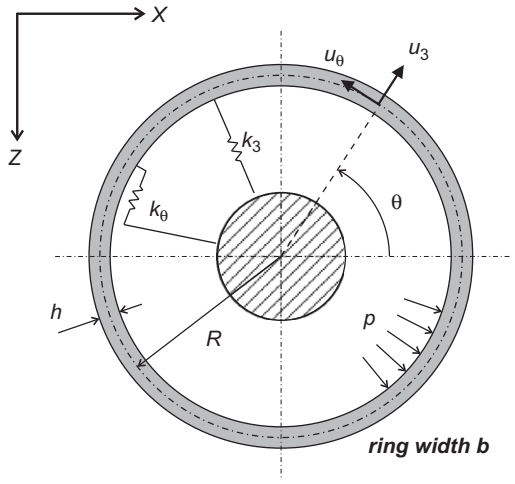

Fig. 1. Flexible ring on elastic foundation with internal pressure.

The stresses and deformations in the y-direction are assumed to be zero ($\varepsilon_{yy}=0, \varepsilon_{\theta y}=0$). Thus, the effect of Poisson's constant is neglected ($\nu=0$). Thirdly, the stress component acting in the normal direction to the neutral surface is neglected. At last, the Love simplifications for thin shells are applied [26]. This implies that the shell in-plane displacements vary linearly through the shell thickness and that the out-of-plane deformation is constant through the shell thickness.

2.2. Natural frequencies

For the eigenvalue analysis, the distributed loads q_3 and q_θ are set equal to zero. At a natural frequency, each point of the ring is moving harmonically which leads to the following expression for the radial and tangential displacement:

$$u_3(\theta,t)=A_n\exp(\mathrm{j}(n\theta+\omega_n t)) \tag{6}$$

$$u_\theta(\theta,t)=B_n\exp(\mathrm{j}(n\theta+\omega_n t)) \tag{7}$$

n is an integer number, representing the circumferential wavenumber. The circumferential orientation of the modes of a perfectly axisymmetric ring is not fixed with respect to the ring. The orientation of a mode is purely dependent on the position of the external force that excites that mode. The proposed displacements in Eqs. (6) and (7) do not consider variations over the width of the ring. This presumption will limit the set of modes that result from this eigenvalue analysis. Substitution of Eqs. (6) and (7) into the equations of motion and elimination of the time dependent portion of the solution leads to two new equations that can be written in matrix form:

$$\begin{bmatrix} M_{11} & M_{12} \\ M_{21} & M_{22} \end{bmatrix} \begin{Bmatrix} A_n \\ B_n \end{Bmatrix} = \{0\} \tag{8}$$

where

$$M_{11}=\left(\frac{Dn^4}{R^4}+\frac{K}{R^2}+\frac{p}{R}(n^2-1)+k_3-\rho h\omega_n^2\right) \tag{9}$$

$$M_{12}=\mathrm{j}\left(\frac{Dn^3}{R^4}+\frac{Kn}{R^2}\right) \tag{10}$$

$$M_{21}=-M_{12} \tag{11}$$

$$M_{22}=\left(\frac{Dn^2}{R^4}+\frac{Kn^2}{R^2}+k_\theta-\rho h\omega_n^2\right) \tag{12}$$

The characteristic equation is obtained by setting the determinant of the above derived coefficient matrix to zero:

$$\omega_n^4+K_1\omega_n^2+K_2=0 \tag{13}$$

with

$$K_1=(-1/\rho h)\left[(k_3+k_\theta)+\frac{p}{R}(n^2-1)+(n^2+1)\left(\frac{Dn^2}{R^4}+\frac{K}{R^2}\right)\right] \tag{14}$$

$$K_2=(1/\rho^2h^2)\left[k_3k_\theta+\frac{K}{R^2}(k_\theta+n^2k_3)+\frac{Dn^2}{R^4}(k_3+n^2k_\theta)+\frac{DK}{R^6}n^2(n^2-1)^2+\frac{p}{R}(n^2-1)\left(\frac{Dn^2}{R^4}+\frac{Kn^2}{R^2}+k_\theta\right)\right] \tag{15}$$

For each value of n, a pair of eigenvalues is found as the roots of Eq. (13). The obtained eigenvalues are the square of the natural frequencies:

$$\omega_{n,1}^2=\tfrac{1}{2}(-K_1-\sqrt{K_1^2-4K_2}) \tag{16}$$

$$\omega_{n,2}^2=\tfrac{1}{2}(-K_1+\sqrt{K_1^2-4K_2}) \tag{17}$$

The mode shape corresponding to each natural frequency can be calculated by substituting Eqs. (16) and (17) into (8) and solving this matrix equation for A_n and B_n. The amplitude ratio of radial and tangential displacement of the mode shape is

derived from one of the two equations of (8)

$$\frac{A_n}{B_n} = \frac{\dfrac{Dn^2}{R^4} + \dfrac{Kn^2}{R^2} + k_\theta - \rho h \omega_n^2}{\mathrm{j}\left(\dfrac{Dn^3}{R^4} + \dfrac{Kn}{R^2}\right)} \tag{18}$$

Eq. (18) shows that for values of $n>1$, the radial component A_n is dominant for the eigenfrequencies $\omega_{n,1}$. For the eigenfrequencies $\omega_{n,2}$, the tangential component B_n is dominant. For values $n \leq 1$, no general conclusion about the nature of the mode shape can be drawn from Eq. (18). At the eigenfrequency $\omega_{0,1}$, the tangential displacement is uniform along the circumference and there is no radial displacement. However, at $\omega_{0,2}$, the radial displacement is uniform along the circumference and there is no tangential displacement. This mode is referred to as the breathing mode of the ring. Some of the modes for $n \leq 1$ are discussed more in detail in Section 2.4.

2.3. Tyre mode naming convention

Fig. 2 explains the naming convention used for the structural tyre mode shapes. An unambiguous naming convention for the modes of an unloaded tyre was proposed by Wheeler et al. [27]. This convention uses two integer indices which describe the bending order of the belt package in the two directions. The format of the notation is (n, a). The first index n represents the number of circumferential bending wavelengths of the belt. The second index a represents the number of half-wavelengths in the axial direction of the belt at a circumferential location where the shape is at an extreme radial displacement. The above described convention is ambiguous for some of the modes in which the belt translates or rotates as a rigid structure. For those modes, an additional label—such as: lateral, pitch, torsion—is added to indicate the rigid body motion of the belt.

2.4. Rigid belt modes

The first modes of a flexible ring on elastic foundation are modes in which the ring mainly translates or rotates as a rigid structure. Three of those modes, which are shown in Fig. 3, will be used to calculate the sidewall stiffness of the presented tyre model. Therefore, an expression for the natural frequency is derived for those three modes.

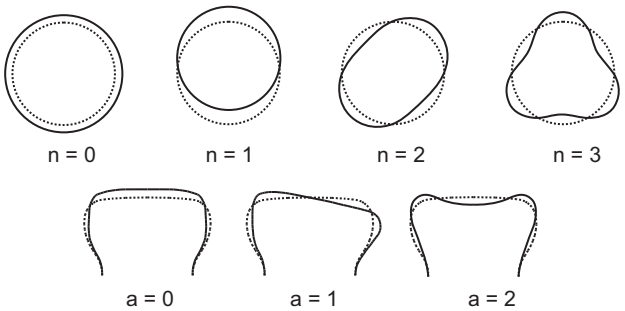

Fig. 2. Naming convention for tyre structural modes (n, a). n: circumferential index; a: belt cross-sectional index.

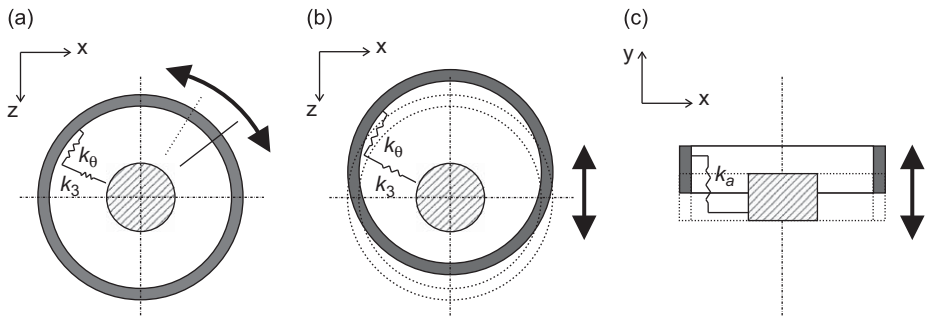

Fig. 3. Rigid ring modes: (a) torsional mode, (b) (1,0) mode and (c) axial mode.

2.4.1. Torsional mode

At the torsional resonance, the ring rotates as a rigid structure around the lateral axis (Fig. 3a). The natural frequency of this mode is derived from Eq. (16) by setting $n = 0$:

$$\begin{aligned}\omega_{\text{torsion}}^2 &= \omega_{0,1}^2 \\ &= \frac{1}{2\rho h}\left((k_3 + k_\theta) + \left(\frac{K}{R^2} - \frac{p}{R}\right) - (k_3 - k_\theta) - \left(\frac{K}{R^2} - \frac{p}{R}\right)\right) \\ &= \frac{k_\theta}{\rho h}\end{aligned} \tag{19}$$

An alternative way to calculate the natural frequency of the torsion mode is to consider the system as a single degree of freedom spring–mass system. The tangential elastic foundation acts as a rotational stiffness and the rigid ring acts as a rotational inertia.

2.4.2. The (1,0) mode

At this resonance, the ring translates as an almost perfectly rigid structure in the plane of the radial and tangential stiffnesses (Fig. 3b). The natural frequency of this mode is derived from Eq. (16) by setting $n = 1$:

$$\begin{aligned}\omega_{(1,0)}^2 &= \omega_{1,1}^2 \\ &= \frac{1}{2\rho h}\left((k_3 + k_\theta) + 2\left(\frac{D}{R^4} + \frac{K}{R^2}\right) - \sqrt{(k_3 - k_\theta)^2 + 4\left(\frac{D}{R^4} + \frac{K}{R^2}\right)^2}\right)\end{aligned} \tag{20}$$

When $k_3 = k_\theta$, Eq. (20) simplifies to

$$\omega_{(1,0)}^2 = \frac{k_3 + k_\theta}{2\rho h} \tag{21}$$

This corresponds to the case in which the ring translates as a perfectly rigid structure. When $k_3 \neq k_\theta$ there will be a slight deformation of the ring at the (1,0) mode and thus, the bending and membrane stiffness of the ring (D and K) influence the resonance frequency.

2.4.3. Axial mode

At the axial resonance, the ring translates as a rigid structure along the lateral axis (Fig. 3c). The natural frequency of this mode cannot be derived from Eq. (16) or (17) because the lateral motion is not included in the equations of motion. However, the system can be considered as a single degree of freedom spring–mass system. The axial elastic foundation acts as stiffness and the rigid ring acts as mass. k_a is the stiffness values per unit area (N m^{-3}) of the distributed axial linear sidewall spring:

$$\omega_{\text{axial}}^2 = \frac{k_a}{\rho h} \tag{22}$$

3. Development of the structural tyre model

This section describes the finite element based structural tyre model of an unloaded tyre, clamped at the wheel spindle. The model is applied to a smooth tyre of size 205/55R16. The model is based on a three-dimensional flexible ring on an elastic foundation. The ring represents the belt and the elastic foundation represents the tyre sidewall. The model, which is implemented in ABAQUS, is valid up to 300 Hz and includes a submodel of the wheel and the air cavity.

3.1. Wheel submodel

The dynamic interaction between tyre and wheel has an effect on the vehicle NVH. Different wheels can produce perceptible differences in vehicle interior noise. In the frequency range 200–350 Hz, differences in interior sound pressure level up to 5 dB were found between a steel wheel and an aluminium wheel [28]. Consequently, the dynamic behaviour of the wheel should be included in the tyre model. In general, the first resonance of a steel wheel (range 150–200 Hz) is much lower compared to an aluminium wheel of the same size (range 300–350 Hz) [27]. As a consequence, most tyre models for interior noise simulations do not include the wheel dynamics when an aluminium wheel is used. In the presented model, a steel wheel with rim diameter 16 in is used. Fig. 4a shows the finite element model of the wheel. Table 1 lists the parameters of the wheel model. The model does not include a damping definition. The geometry of the wheel is modelled in detail because the flexibility of rim and disk are highly influenced by their complex shape. An attempt was made to use a geometrically simplified wheel model; however, the dynamic behaviour could not be accurately described. An eigenvalue

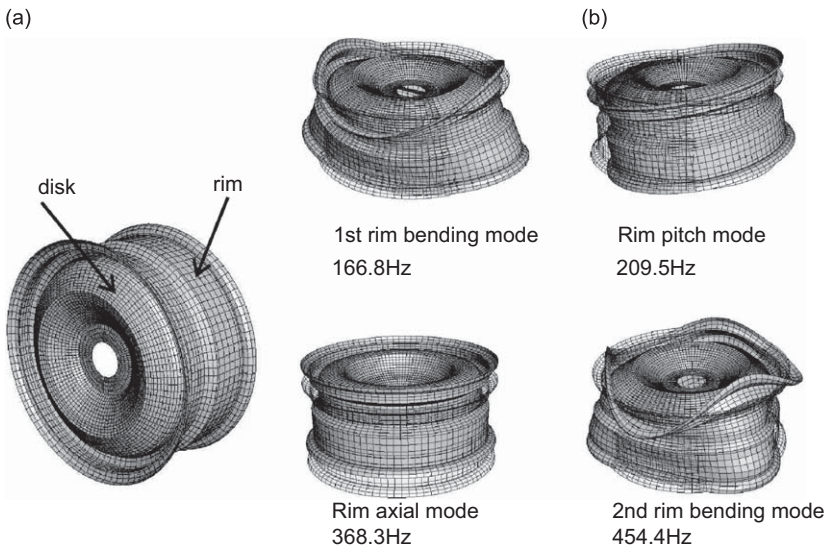

Fig. 4. (a) Finite element model of the steel wheel. (b) Mode shape and natural frequency of the first four calculated wheel resonances.

Table 1
Parameters of the steel wheel model.

Parameter	Description	Value
t_{rim}	Plate thickness of rim	2 mm
t_{disk}	Plate thickness of disk	3.3 mm
E	Elastic modulus of steel	210×10^9 N m^{-2}
v	Poisson's ratio of steel	0.3
ρ	Density of steel	7800 kg m^{-3}
m_{wheel}	Total mass of the wheel	8.34 kg

Table 2
Comparison between calculated and measured clamped wheel resonance frequencies.

Wheel mode	FEM model	Experimental modal test	
	Freq. (Hz)	Freq. (Hz)	Mod. damping (%)
1st bending	166.8	167.5	0.09
Pitch	209.5	205.5	0.10
Axial	368.3	393.2	0.35
2nd bending	454.4	440.7	0.14

analysis was performed on the wheel model, clamped at the spindle. Fig. 4b shows the first four calculated wheel modes. Table 2 makes a comparison between the results from the finite element calculation and an experimental modal analysis. This comparison shows that the wheel model is sufficiently accurate in the frequency range of interest. The total mass of the wheel model also corresponds to the measured total mass. This total mass is of importance when the tyre model is used in a full vehicle model in which the wheel mass contributes to the unsprung mass of the vehicle suspension.

3.2. Treadband ring submodel

A radial tyre is composed of radial plies (carcass) that are enclosed by a steel reinforced belt and tread layer. Due to the orientation of the rubberized plies and the steel wires in the belt, the tyre treadband exhibits orthotropic behaviour. The circumferential stiffness of the treadband is generally higher than the cross-sectional stiffness. In the presented tyre model, the treadband is modelled as an isotropic three-dimensional ring. Despite this drastic simplification, the tyre model

Table 3
Parameters of the treadband ring model.

Parameter	Description	Value
R_{out}	Tyre outer radius	0.316 m
h	Treadband thickness	14.1 mm
b	Treadband width	0.185 m
E'	Elastic storage modulus	4.5×10^8 N m^{-2}
η	Loss factor	0.15
v	Poisson's ratio	0.45
ρ	Density	1452 kg m^{-3}

exhibits acceptable accuracy in the frequency range of interest, as will be shown in the results and validation section of this paper. The assumption of isotropy is reasonable for the two types of modes the model describes.

As a general engineering approach, energy dissipation in a structure is approximated by a mathematical model. However, for complex structures such as tyres, it is not obvious which damping model is most appropriate. Geng et al. [29] showed that the commonly used simplification of proportional viscous damping does not provide an adequate description of the physical energy dissipation in tyres. A more general viscous damping distribution is needed, which results in a more complex identification of the damping model.

The nonlinear static material behaviour of the ring is described by the Neo-Hookean hyperelastic material model. This model is applicable for incompressible and nearly incompressible materials and is commonly used when no accurate material data is available. Since energy dissipation in rubberlike materials has a hysteretic character, their dynamic characteristics are often expressed as a complex dynamic shear modulus G^* and complex Young's modulus E^*. The complex Poisson's ratio v^* defines the relation between the complex dynamic shear and Young's modulus [30]:

$$E^* = E' + jE'' = 2(1 + v^*)G^* \tag{23}$$

The dynamic moduli from viscoelastic materials are found to be strongly dependent on frequency, temperature and vibration amplitude. The imaginary part of Poisson's ratio is small compared to the real part and therefore can be neglected [31]. Thus, the viscoelastic material is dynamically unambiguously characterized by the real Poisson's ratio and the complex Young's modulus. The real part E' is referred to as the storage modulus, whereas the imaginary part E'' is referred to as the loss modulus. The damping can be expressed by the ratio between imaginary and real part of the complex Young's modulus, which is referred to as the loss factor:

$$\eta = \frac{E''}{E'} \tag{24}$$

In this tyre model, the material properties of the treadband are considered to be frequency independent. This corresponds to proportional hysteretic damping and is a widely used assumption for structure-borne sound applications in the frequency range of interest. This material model is only valid for steady-state harmonic vibrations since it can lead to non-causal transient solutions. The values for the loss factor and Poisson's ratio are obtained from literature [8,10] and have proven to be a good assumption. The elastic storage modulus is tuned by adjusting its value in order to reduce the error on the predicted natural frequencies. A sensitivity analysis showed that the modes with a circumferential index $n<3$ are nearly insensitive to the elastic storage modulus.

The parameters of the ring are listed in Table 3. The ring is discretized in the finite element model by 4-node shell elements (ABAQUS S4R elements). The elements allow transverse shear deformation and account for finite membrane strains and arbitrarily large rotations. Ninety elements are used in the circumferential direction and 12 elements in the axial direction. A convergence analysis confirmed that this mesh is sufficiently dense in the frequency range of interest.

3.3. Tyre sidewall submodel

The tyre sidewalls are approximated by distributed spring–damper systems in radial, tangential and axial direction. The sidewall stiffness is composed of a structural contribution and a pressurized membrane contribution. The structural contribution originates from the bending, shear and tensile stiffness of the sidewall. The pressurized membrane contribution originates from the fact that during a deflection of the sidewall, work is done against the inflation pressure [18].

The elastic foundation is distributed along the circumference at both edges of the treadband ring. The sidewall springs have a fixed direction such that they only oppose displacements in their respective direction. Consequently, the radial springs do not rotate together with the treadband ring. An experimental modal analysis on an unloaded tyre, clamped at the spindle, shows that the first four resonances behave like a spring–mass system in which the sidewall acts as a spring and the treadband as a mass [32]. Therefore, the tyre behaviour can be approximated as a ring on an elastic foundation and Eqs. (19), (21) and (22) can be used to calculate the sidewall stiffness from the undamped natural frequency of the

Table 4
Experimental tyre modal parameters of torsional, (1,0) and axial mode.

Tyre mode	Experimental modal test	
	Freq. (Hz)	Mod. damping (%)
Axial	47.20	1.87
Torsion	74.25	6.39
(1,0)	91.26	4.49

Table 5
Sidewall stiffness and damping constants (values per unit of ring area).

Parameter	Description	Value
k_3	Radial sidewall stiffness	$9.0 \times 10^6\,\mathrm{N\,m^{-3}}$
c_3	Radial sidewall viscous damping	$885\,\mathrm{N\,s\,m^{-3}}$
k_θ	Tangential sidewall stiffness	$4.47 \times 10^6\,\mathrm{N\,m^{-3}}$
c_θ	Tangential sidewall viscous damping	$1222\,\mathrm{N\,s\,m^{-3}}$
k_a	Axial sidewall stiffness	$1.80 \times 10^6\,\mathrm{N\,m^{-3}}$
c_a	Axial sidewall viscous damping	$227\,\mathrm{N\,s\,m^{-3}}$

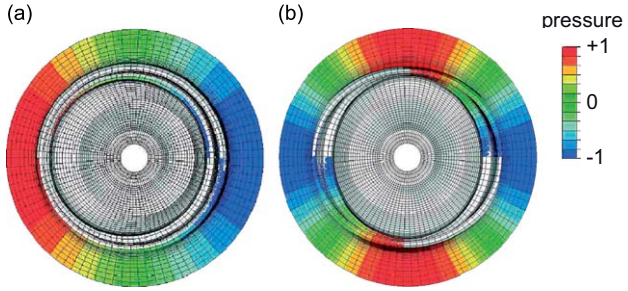

Fig. 5. Acoustic pressure distribution inside the tyre air cavity at resonance: (a) first acoustic cavity mode and (b) second acoustic cavity mode.

torsional, (1,0) and axial mode, respectively. Table 4 lists the measured resonance frequency and modal damping—expressed as a fraction of the critical damping—of the torsional, (1,0) and axial mode. This modal test can be performed relatively fast and only two tri-axial accelerometers are required to make a distinction between the different modes. From these modal parameters, the distributed linear spring constant k and viscous damping constant c of the sidewall can be calculated using Eq. (25). This equation describes the relation between the undamped natural frequency ω, damped natural frequency Ω and damping ratio ξ for a single degree of freedom system. k, c and m are the stiffness, damping and mass of the single degree of freedom system, respectively:

$$\Omega = \left(\sqrt{1-\xi^2}\right)\omega \quad \text{with } \xi = \frac{c}{2\sqrt{km}} \text{ and } \omega = \sqrt{\frac{k}{m}} \tag{25}$$

The calculated sidewall spring and damping constants are shown in Table 5 and are calculated per unit area of the treadband ring.

The calculation of the radial sidewall stiffness is based on Eq. (21), which is valid when $k_3 = k_\theta$. Although this assumption is not satisfied here, the difference on the radial stiffnesses, calculated with Eqs. (20) and (21) is found to be 0.4 percent for the presented tyre. This demonstrates the validity of Eq. (21) for the calculation of the tyre sidewall stiffness.

The above presented sidewall model is based on the assumption that the dynamic behaviour of the sidewall can be described by means of a spring–damper system. This simplifies the parametrization of the tyre model significantly. However, it limits the model to the prediction of the $(n,0)$ and $(n,1)$ modes (Fig. 2). For the cross-sectional bending modes of higher order ($a \geq 2$), the sidewall dynamic behaviour deviates too much from a spring–damper system. Unlike the real tyre sidewall, the presented simplified sidewall model has no mass. Therefore, half of the sidewall mass is assigned to both the treadband ring and the wheel rim.

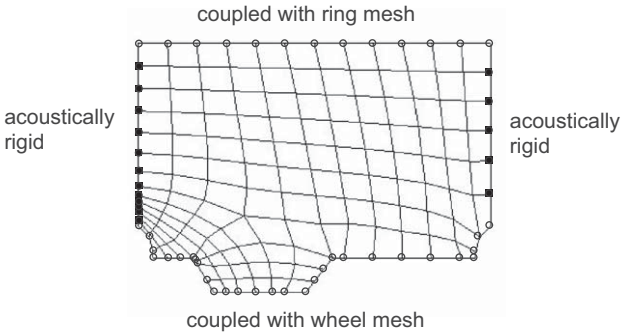

Fig. 6. Cross-section of the tyre air cavity acoustic mesh.

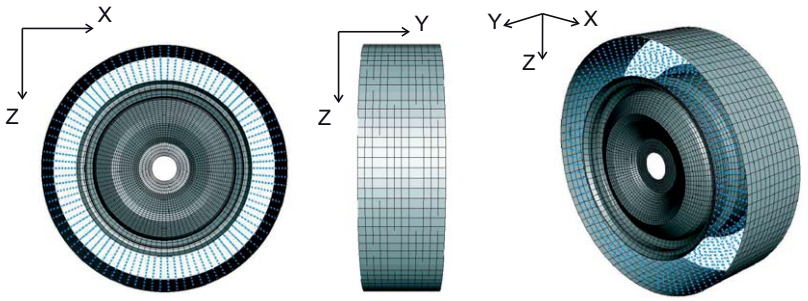

Fig. 7. Fully assembled tyre–wheel model (cavity mesh is not shown).

3.4. Air cavity submodel

The tyre structural behaviour is significantly affected by the presence of the inner air cavity [33]. Fig. 5 shows the acoustic pressure distribution inside the tyre air cavity at the first and second acoustic cavity resonance. The first cavity resonance for an unloaded tyre appears in the frequency range between 200 and 250 Hz. The air cavity acoustic resonances also appear as distinct narrow peaks in the spectrum of the vehicle interior noise [11]. Therefore, the structural–acoustic coupling between tyre and air cavity is included in the presented tyre model.

The air cavity is discretized using 8-node linear brick acoustic elements and is coupled to the structural mesh of the wheel and treadband ring. The sidewalls of the cavity are considered to be acoustically rigid. Fig. 6 shows a cross-section of the acoustic mesh, which has 90 acoustic elements in the circumferential direction. The values of the bulk modulus and the density of air are taken to be 450 kPa and 3.818 kg m^{-3}, respectively, and represent the properties of air at a temperature of 20 °C and a relative pressure of 2.2×10^5 Pa. The cavity model does not include a damping definition. Typically, the loss factor for the air in the tyre is a factor 100 smaller than the loss factor of the tyre tread [34].

3.5. Tyre–wheel assembly

Fig. 7 shows the fully assembled tyre model. For clarity, the cavity mesh is not depicted. First, a static analysis of the tyre inflation is performed. The wheel centre is clamped and the tyre is inflated to 2.2×10^5 Pa in a geometric nonlinear analysis. The inflation pressure is applied to the rim outer surface and the treadband ring inner surface. This pressure loading induces a circumferential pretension in the ring which significantly contributes to the tyre stiffness (see Section 2). Besides the circumferential tension, the tyre treadband is also subjected to an axial tension. This tension is not induced by the inflation pressure in the model and therefore this tension will be applied as an external loading. The calculation of the axial tension is based on a model in which the sidewall is represented as an inextensible membrane with circular section [35]. Fig. 8 shows a schematic representation of the half tyre cross-section. The static horizontal equilibrium of the half treadband gives

$$N^r_{yy} - T_s \sin(\theta_s/2) = 0 \tag{26}$$

where N^r_{yy} represents the axial tensile force of the ring per unit circumferential length. θ_s is the angle of the circular section with radius R_s that represents the sidewall. The static horizontal equilibrium of the sidewall yields an expression for the

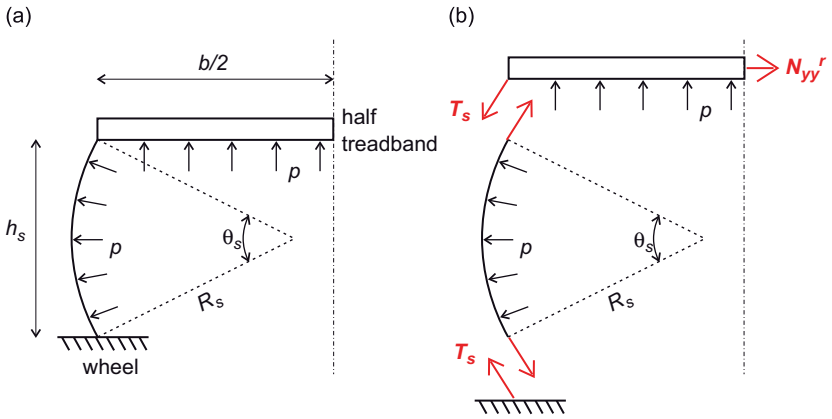

Fig. 8. Schematic representation of half tyre cross-section: (a) geometry and (b) sidewall tension T_s and axial ring tension N_{yy}^r.

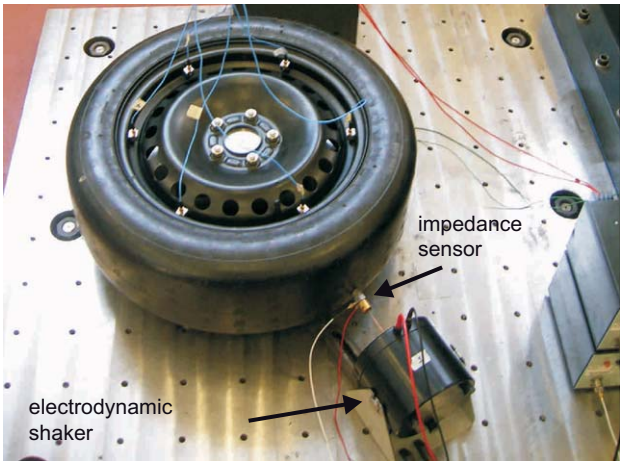

Fig. 9. Test set-up for the experimental modal analysis on the unloaded tyre.

sidewall tensile force T_s per unit circumferential length:

$$T_s = \frac{ph_s}{2\sin(\theta_s/2)} \tag{27}$$

where h_s and p are the sidewall height and the tyre inflation pressure, respectively. Substitution of Eq. (27) into (26) yields

$$N_{yy}^r = \frac{ph_s}{2} \tag{28}$$

For a tyre sidewall height of 0.075 m and an inflation pressure of 2.2×10^5 Pa, the axial tensile force N_{yy}^r becomes $8250\,\mathrm{N\,m^{-1}}$.

4. Results and validation

The presented tyre model will be validated by comparing measured and calculated frequency response functions (FRFs) and modal parameters. The response calculations in this section assume the tyre to be linear. Once the tyre is inflated, this is a valid assumption within a wide range of excitations [29].

4.1. Complex eigenvalue analysis

After the static analysis in which the tyre is inflated, an eigenvalue analysis is performed in which the first 80 undamped eigenvalues of the tyre model are calculated. This analysis is followed by a complex eigenvalue extraction, based on the

Table 6
Comparison between measured and calculated modal parameters.

Mode	Test		Model	
	Freq. (Hz)	Damping (%)	Freq. (Hz)	Damping (%)
Axial*	47.2	1.87	47.5	1.51
(1,1)	56.9	2.14	53.1	1.42
Torsion*	74.3	6.39	74.0	6.05
(2,1)	89.4	2.07	85.6	1.95
(1,0)*	91.3	4.49	91.2	3.48
(2,0)	118.5	3.26	114.8	3.08
(3,0)	142.0	2.78	137.7	2.79
(4,0)	170.0	3.01	165.9	3.11
(3,1)	171.9	2.73	169.8	4.33
1st rim bending	187.2	2.12	184.2	3.36
Rim pitch	189.9	0.69	189.3	1.47
(5,0)	201.8	2.41	201.3	3.96
(4,1)	222.9	3.57	223.0	5.45
1st acoustic	225.8	0.25	228.0	0.89
(6,0)	233.8	2.82	244.5	5.34
(5,1)	252.6	4.13	267.9	6.73
(7,0)	268.9	2.98	295.7	7.26

*Indicates a mode that is used in the parameterization of the model.

Lanczos subspace projection method [36]. This method is an iterative Krylov subspace method. The real eigenvectors of the undamped eigenvalue analysis are used to define the projection subspace. Stiffness and damping properties cannot be modified during an eigenvalue calculation, thus the frequency dependent material properties have to be evaluated at a specific frequency. In this model, the complex Young's modulus is constant for all frequencies; therefore, the solution will not depend on the evaluation frequency.

An experimental modal analysis is performed on the unloaded tyre–wheel assembly. The wheel is clamped at a spindle (Fig. 9) which can be considered rigid in the frequency range of interest. Thus, the boundary condition of the simulation is well approximated in the measurement. The tyre is excited by an electrodynamic shaker (Brüel and Kjaer 4809), connected to the tyre surface through a stinger and a 10 mm diameter metal disk which is glued to the tyre tread surface. The excitation force and acceleration in the excitation point are measured by an impedance sensor (PCB 288D01). A burst random signal, with frequency range of 0–1024 Hz and burst time of 80 percent of the excitation period, is amplified and delivered to the shaker. In order to excite all tyre modes in the frequency range of interest, the shaker is aligned such that excitation is provided in radial, tangential and axial direction. Tri-axial accelerometers (PCB 356A15) are used to measure the response of points on the treadband and wheel.

Comparison of the calculated damped natural frequencies with the measured natural frequencies shows that the calculated natural frequencies are underestimated. This is a result of the parametrization of the tyre sidewall (Section 3.3) in which the flexibility of the wheel and the acoustic coupling are not taken into account. Therefore, the sidewall stiffness values have to be increased in order to obtain the correct natural frequencies for the torsional, (1,0) and axial mode. First, the axial and tangential sidewall stiffness values have to be updated separately, based on the natural frequency of the axial and torsional mode, respectively. The axial mode is predominantly influenced by the axial sidewall stiffness, whereas for the torsional mode it is the tangential sidewall stiffness. Finally, the radial stiffness has to be updated, based on the natural frequency of the (1,0) mode. This natural frequency is mainly dependent on the tangential and radial stiffness; however, only the radial stiffness has to be updated because the tangential stiffness has already been updated, based on the torsional mode. In this way, the three sidewall stiffness values can be updated independently. For the model of the smooth tyre, the axial, tangential and radial stiffness calculated by the analytical model has to be increased by 13, 4.5 and 34 percent, respectively, in order to obtain the measured natural frequency for the torsional, (1,0) and axial mode. If the wheel flexibility and the acoustic coupling are included in the analytical model, no corrections on the calculated stiffnesses would be required.

Table 6 gives a comparison between the measured and calculated modal parameters up to 300 Hz. The eigenfrequency predictions are within five percent, except for the (1,1) mode (error −6.9 percent), the (5,1) mode (error +6.1 percent) and the (7,0) mode (error +9.9 percent). The increasing error on the last two modes is caused by the cross-sectional bending modes of higher order ($a>1$) which start to appear between 300 and 350 Hz. The presented model cannot describe those modes correctly as the sidewall dynamic behaviour of those modes deviates too much from a spring–damper system.

Fig. 10 compares some of the measured mode shapes with calculated mode shapes of the model. The air cavity is not shown because no acoustic pressure measurements in the cavity were performed during the experimental modal test. The calculated and measured mode shapes show good agreement. All calculated modes were identified in the modal test and vice versa. Most poles are found to be double as the unloaded tyre is axisymmetric.

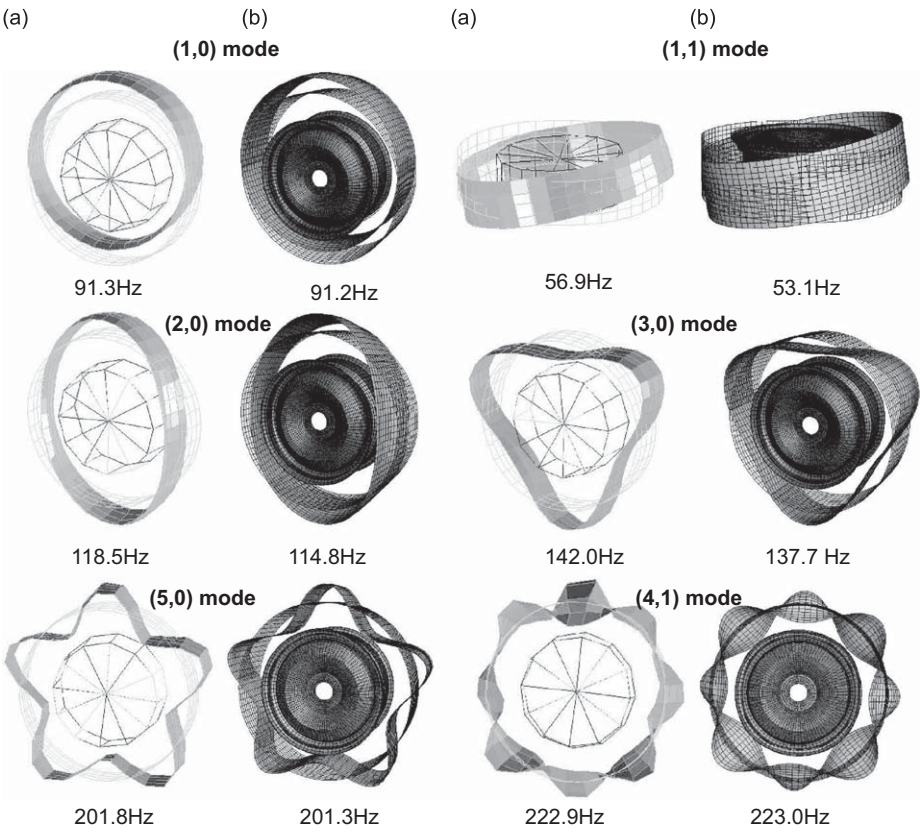

Fig. 10. Comparison between measured (a) and calculated (b) mode shapes.

4.2. Steady-state harmonic analysis

This analysis calculates the steady-state linearized response of the tyre–wheel model to a harmonic excitation at the treadband. The response is calculated up to 300 Hz. Rather than a direct calculation, in which the response is calculated in terms of the physical degrees of freedom of the model using the mass, damping and stiffness matrices, a subspace-based method is used here to calculate the harmonic response. This approach is computationally less expensive than a direct calculation and is still able to include frequency-dependent material properties. Fig. 11 compares the measured and calculated inertance frequency response function of the radial, tangential and axial response due to a harmonic force. The position of the excitation force and the response point is indicated next to the graphs. The differences between measured and calculated FRFs are acceptable. The largest errors appear around anti-resonances, as the response is there most sensitive to position errors of the accelerometers. Both the measured and calculated FRF of the tangential response show a distinct peak around 225 Hz, which corresponds to the first air cavity resonance.

Fig. 12 compares the measured and calculated point mobility FRF. Besides a frequency shift on certain modes, the agreement is good. The measurement of a tyre point mobility is highly sensitive to mass loading, rotational inertia, moment excitation and constraints on displacement due to the impedance sensor which is mounted on the tyre surface. Therefore, the measured mobility should be compensated [37] or the sensor mounting effects should be modelled, in order to be able to compare measured and calculated mobility. However, both methods require additional measurements to characterise the sensor mounting effects. Therefore, the measured mobility of Fig. 12 was obtained by hammer excitation, combined with a contactless response measurement by a laser Doppler vibrometer. The most important drawback of this approach is the high uncertainty on the hammer excitation direction.

4.3. Influence of wheel and air cavity

The above presented results show that the tyre–wheel model describes the dynamic behaviour up to 300 Hz with acceptable accuracy. The nature of this model makes it less suited to assess the influence of detailed tyre parameter changes onto the tyre structural response. Nevertheless, all model parameters have a physical meaning and can be linked to tyre design parameters. This section analyses the influence of the wheel flexibility and the air cavity on the structural behaviour.

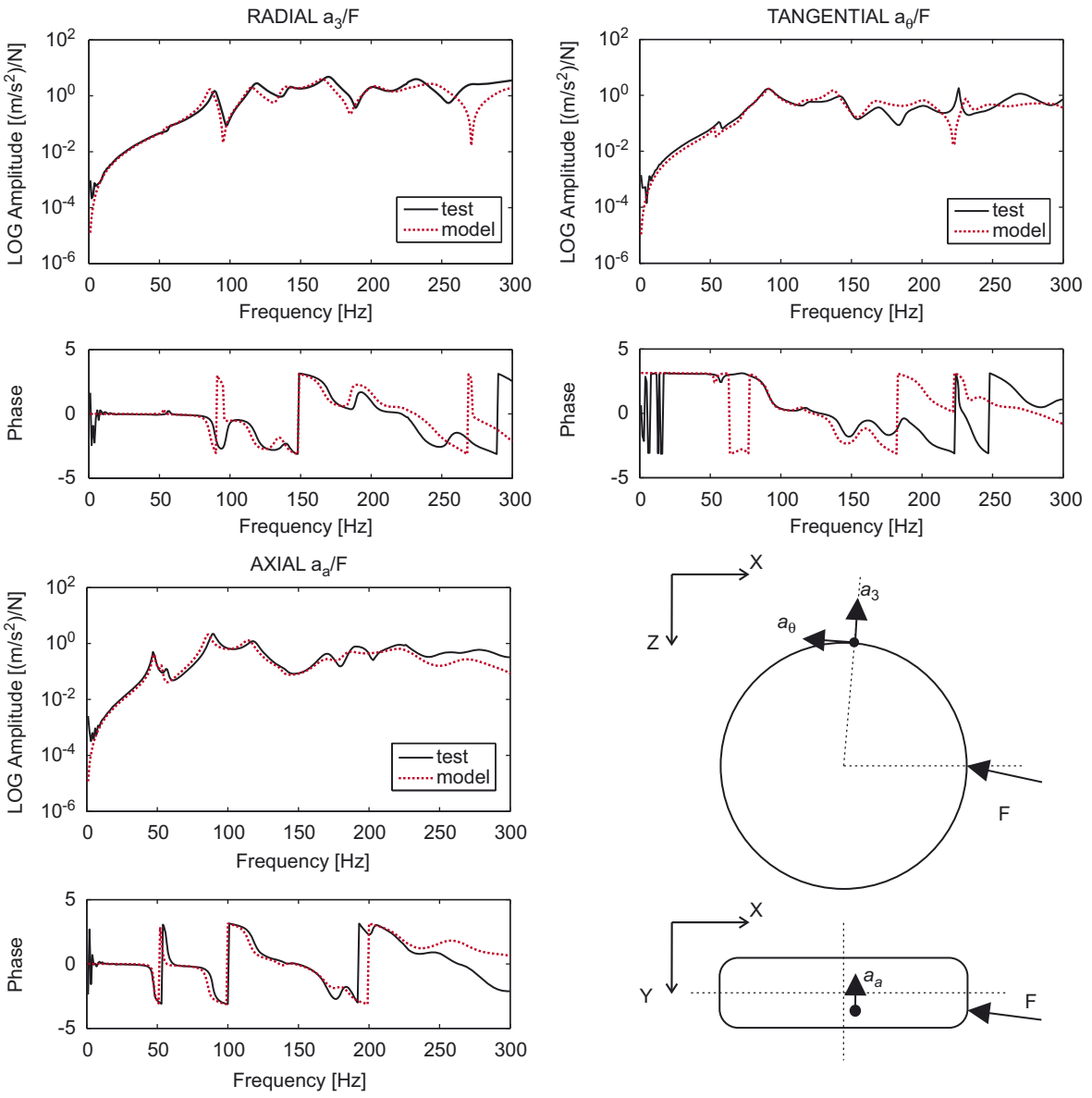

Fig. 11. Magnitude and phase of inertance FRF. Measured (solid) and calculated (dashed).

Table 7 lists the influence of two hypothetical assumptions on the predicted resonance frequencies of the model. The first assumption is an infinitely rigid wheel and the second assumption is a tyre in which the air cavity has no dynamic behaviour. From both experimental as calculated mode shapes, a coupling between certain modes can be observed. A strong coupling is observed between the (2,1) mode and the first rim bending mode (Fig. 13). This coupling explains the strong influence of the wheel stiffness onto the (2,1) resonance frequency. A similar coupling effect is present between the (1,1) mode and the rim pitch mode. Table 7 shows that the $(n,1)$ modes are more influenced by the wheel stiffness compared to their corresponding $(n,0)$ mode. Fig. 14 shows the point mobility of a model with a flexible and rigid wheel. This figure shows almost no influence of the wheel flexibility in the frequency region where the wheel modes appear (180–190 Hz). However, the influence below 150 Hz is significant due to tyre modes that couple with the wheel modes. The predicted influences of the wheel flexibility correspond exactly with the findings from Wheeler et al. [27], who performed an experimental modal analysis on a tyre with a standard steel wheel and a stiffened steel wheel.

Fig. 15 compares the point mobility of the model with and without air cavity. The dynamic behaviour of the air cavity has a much smaller influence on the point mobility as compared to the wheel dynamic behaviour. Table 7 shows that only the (1,0) and rim pitch resonance frequency are significantly affected by the air cavity. Those two modes are found to have the strongest coupling with the first acoustic cavity resonance. Fig. 16 shows the acoustic pressure distribution at the (1,0) and rim pitch resonance. This pressure distribution clearly corresponds to the pressure distribution at the first cavity

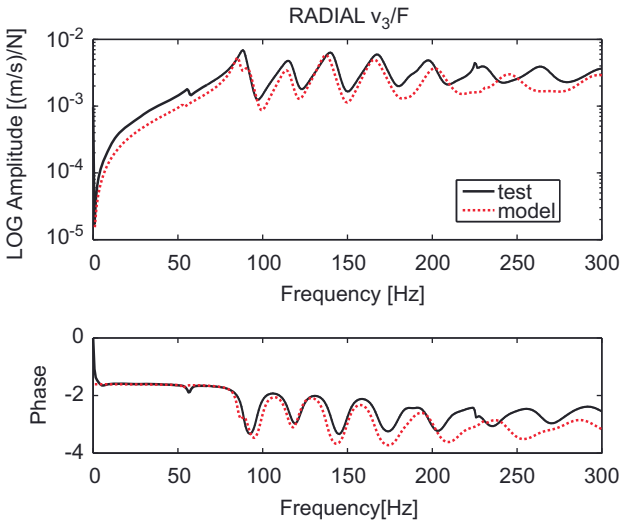

Fig. 12. Magnitude and phase of point mobility FRF. Measured (solid) and calculated (dashed).

Table 7
Influence of wheel flexibility and air cavity on the calculated resonance frequencies.

Mode	Original model	Rigid wheel	No air cavity
	Freq. (Hz)	Deviation (%)	Deviation (%)
Axial	47.5	+5.3	0.0
(1,1)	53.1	+13.0	0.0
Torsion	74.0	+1.4	0.0
(2,1)	85.6	+30.3	+0.2
(1,0)	91.2	+3.7	+3.4
(2,0)	114.8	+2.2	+1.2
(3,0)	137.7	+1.2	+1.0
(4,0)	165.9	+0.6	+0.7
(3,1)	169.8	+4.4	+0.3
1st rim bending	184.2	*	+0.7
Rim pitch	189.3	*	+2.0
(5,0)	201.3	+0.2	+0.6
(4,1)	223.0	+1.9	+0.4
1st acoustic	228.0	−1.4	*
(6,0)	244.5	+0.1	+0.5
(5,1)	267.9	+1.0	+0.4
(7,0)	295.7	+0.1	+0.4

*Indicates a mode that is not predicted by the model.

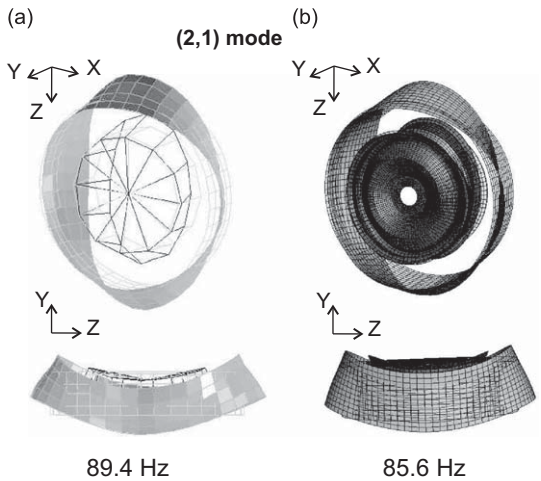

Fig. 13. Coupling between (2,1) mode and first wheel bending mode (measured (a) and calculated (b) mode shape).

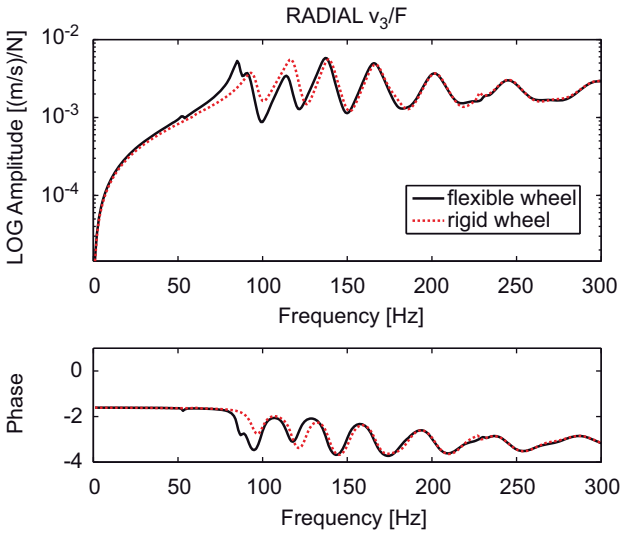

Fig. 14. Influence of wheel flexibility on the point mobility FRF.

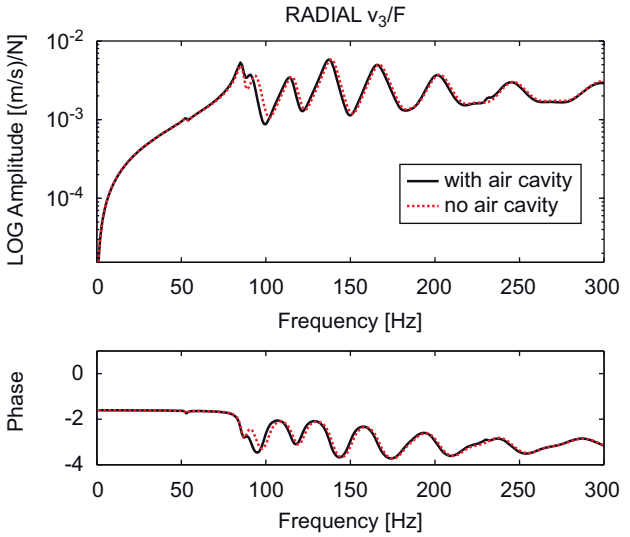

Fig. 15. Influence of air cavity on the point mobility FRF.

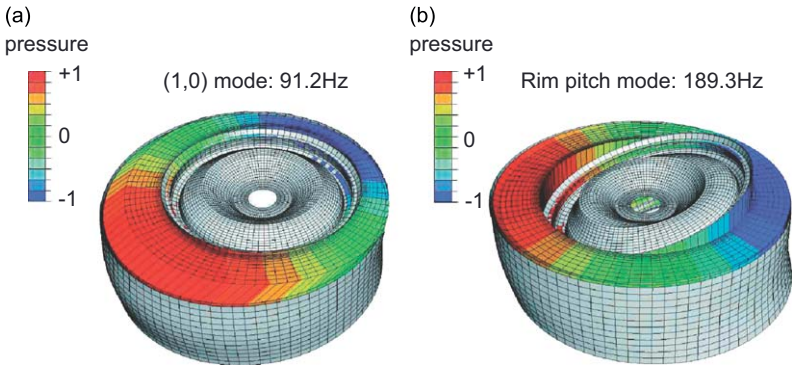

Fig. 16. Acoustic pressure distribution in the air cavity at the (1,0) mode (a) and rim pitch mode (b).

resonance (Fig. 5). Although the air cavity geometry is simplified and the coupling with the tyre sidewalls is neglected in this model, the same conclusions are found from detailed tyre finite element models [27].

5. Conclusions

This paper describes a physically based structural tyre model for the analysis of the tyre dynamic behaviour up to 300 Hz. The model describes all modes that appear in this frequency range, unlike most ring models that are limited to in-plane modes. The main assumption is that the dynamic behaviour of a tyre in this frequency range can be approximated by a flexible three-dimensional ring on an elastic foundation. The model is implemented as a finite element model. The fully assembled tyre model includes a wheel and air cavity model, which is necessary to describe all physical phenomena below 300 Hz. It has been shown in this paper that the wheel flexibility has a significant influence on the lowest tyre modes. Therefore, a detailed wheel model is needed to obtain the required accuracy of the fully assembled model.

The parametrization of the model is based on simple geometrical properties of the tyre and the experimental modal parameters of three tyre modes. Despite the drastic, well considered simplifications, comparison between measured and calculated responses shows that the tyre–wheel model describes the dynamic behaviour with acceptable accuracy.

Because the model is physical, it can also be applied to predict the dynamic behaviour under different operating conditions, such as loading and rotation. However, a more detailed description of the treadband and a nonlinear sidewall stiffness formulation might be considered in this case. A next step in the ongoing research is to implement those applications of the tyre model.

Acknowledgement

The reported research is funded by a PhD grant of the Institute for the Promotion of Innovation through Science and Technology in Flanders (IWT-Vlaanderen).

Appendix A. Circumferential tension in ring due to internal pressure

This appendix derives an expression for the circumferential pretension in the ring due to the internal pressure on the ring. Consider an elementary ring fragment composed of the angle $\mathrm{d}\theta$ (see Fig. A1). The static equilibrium of the ring fragment can be written as

$$F_3^r - 2\sin(\mathrm{d}\theta/2)N_{\theta\theta}^r = 0 \tag{A.1}$$

$N_{\theta\theta}^r$ represents the pretension force resultant in the ring per unit width of the ring. Because the angle $\mathrm{d}\theta$ is small, the term $\sin(\mathrm{d}\theta/2)$ can be approximated by $\mathrm{d}\theta/2$. When the ring is subjected to an internal pressure p and a rotation with constant angular velocity Ω, the force resultant F_3^r becomes

$$F_3^r = p(R\,\mathrm{d}\theta) + (\rho hR\,\mathrm{d}\theta)R\Omega^2 - k_3(R\,\mathrm{d}\theta)u_3 \tag{A.2}$$

The first, second and third term represent the force resultant due to the internal pressure, centrifugal acceleration and deformation of the radial springs, respectively. By assuming that the pretension is constant through the shell thickness, the static radial displacement u_3 can be approximated by

$$u_3 \approx N_{\theta\theta}^r R/(hE) \tag{A.3}$$

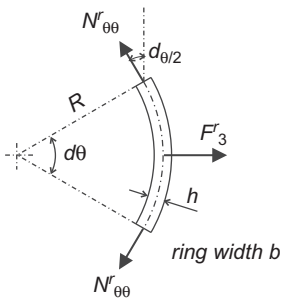

Fig. A1. Static force equilibrium of an elementary ring fragment.

Substituting Eqs. (A.2) and (A.3) into Eq. (A.1) yields

$$N^r_{\theta\theta} \approx \frac{pR + \rho R^2 h\Omega^2}{1 + k_3 R^2/(hE)} \tag{A.4}$$

For a non-rotating ring, Eq. (A.4) simplifies to

$$N^r_{\theta\theta} \approx \frac{pR}{1 + k_3 R^2/(hE)} \tag{A.5}$$

Poisson's constant is assumed to be zero in the above derived expression. This assumption is justified for the application presented in this paper, since the difference between the exact and the approximated pretension is found to be 2.4 percent.

References

[1] S. Sandrock, B. Griefahn, T. Kaczmarek, H. Hafka, A. Preis, T. Gjestland, Experimental studies on annoyance caused by noises from trams and buses, *Journal of Sound and Vibration* 313 (2008) 908–919.
[2] J. Lambert, Report on noise exposure of the population, health risks and social welfare costs, *Proceedings of the Noise in Europe Conference*, Paris, France, 2000.
[3] E. Öhrström, A. Skanberg, H. Svensson, A. Gidlöf-Gunnarsson, Effects of road traffic noise and the benefit of access to quietness, *Journal of Sound and Vibration* 295 (2006) 40–59.
[4] Study SI2.408210 tyre/road noise, Technical Report, Forum of European National Highway Research Laboratories (FEHRL), 2006 ⟨http://ec.europa.eu/enterprise/automotive/projects⟩.
[5] U. Sandberg, J.A. Ejsmont, Tyre/road noise reference book, Informex, SE-59040, Kisa, Sweden, 2002.
[6] B.S. Kim, G.J. Kim, T.K. Lee, The identification of tyre induced vehicle interior noise, *Applied Acoustics* 68 (1) (2007) 134–156.
[7] K. Larrson, W. Kropp, A high-frequency three-dimensional tyre model based on two coupled elastic layers, *Journal of Sound and Vibration* 253 (4) (2002) 889–908.
[8] R.J. Pinnington, A.R. Briscoe, A wave model for a pneumatic tyre belt, *Journal of Sound and Vibration* 253 (5) (2002) 941–959.
[9] W. Kropp, K. Larsson, F. Wullens, P. Andersson, F.X. Becot, The generation of tyre/road noise mechanisms and models, *Proceedings of the International Congress on Sound and Vibration*, *ICSV* 10, Stockholm, Sweden, 2003.
[10] Y.J. Kim, J.S. Bolton, Effects of rotation on the dynamics of a circular cylindrical shell with application to tire vibration, *Journal of Sound and Vibration* 275 (2004) 605–621.
[11] T. Sakata, H. Morimura, H. Ide, Effects of tire cavity resonance on vehicle road noise, *Tire Science and Technology, TSTCA* 18 (2) (1990) 68–79.
[12] L.G. Hartleip, T.J. Roggenkamp, Case study—experimental determination of airborne and structure-borne road noise spectral content on passenger vehicles, *Proceedings of SAE Noise and Vibration Conference*, Traverse City, USA, 2005, paper 2005-01-2522.
[13] A. Kuijpers, G. Blokland, Tyre/road noise models in the last two decades: a critical evaluation, *Proceedings of Internoise* 2001, The Hague, The Netherlands, 2001.
[14] S. Gong, A Study of In-plane Dynamics of Tires, Ph.D. Thesis, Delft University of Technology, 1993.
[15] W. Soedel, Free vibration of a pneumatic tire–wheel unit using a ring on an elastic foundation and a finite element model, *Journal of Sound and Vibration* 107 (2) (1986) 181–194.
[16] D.J. O'Boy, Tyre/road Noise—Vibration of the Tyre Belt, Ph.D. Thesis, Sidney Sussex College, University of Cambridge, 2005.
[17] P. Andersson, K. Larsson, Validation of a high frequency three-dimensional tyre model, *Acta Acustica united with Acustica* 91 (1) (2005) 121–131.
[18] J.M. Muggleton, B.R. Mace, M.J. Brennan, Vibrational response prediction of a pneumatic tyre using an orthotropic two-plate wave model, *Journal of Sound and Vibration* 264 (2003) 929–950.
[19] W. Hall, J.T. Mottram, R.P. Jones, Tire modeling methodology with the explicit finite element code LS-DYNA, *Tire Science and Technology, TSTCA* 32 (4) (2004) 236–261.
[20] G. Meschke, H.J. Payer, H.A. Mang, 3D simulations of automobile tires, mesh generation and solution strategies: material modeling, *Tire Science and Technology, TSTCA* 25 (3) (1997) 154–176.
[21] M. Brinkmeier, U. Nackenhorst, S. Petersen, O. von Estorff, A finite element approach for the simulation of tire rolling noise, *Journal of Sound and Vibration* 309 (2008) 20–39.
[22] Y.J. Kim, J.S. Bolton, Analysis of tire vibration by using a hybrid two-dimensional finite element based on composite shell theory, *Proceedings of the Internoise* 2003 *Conference*, Jeju, Korea, 2003.
[23] D. Bozdog, W.W. Olson, An advanced shell theory based tire model, *Tire Science and Technology, TSTCA* 33 (4) (2005) 227–238.
[24] I. Lopez, R.E.A. Blom, N.B. Roozen, H. Nijmeijer, Modelling vibrations on deformed rolling tyres—a modal approach, *Journal of Sound and Vibration* 307 (2007) 481–494.
[25] C.M. Nilsson, Waveguide Finite Elements Applied on a Car Tyre, Ph.D. Thesis, KTH Royal Institute of Technology, Department of Aeronautical and Vehicle Technology, Stockholm, 2004.
[26] W. Soedel, *Vibrations of Shells and Plates*, third ed., Marcel Decker, New York, 2004.
[27] R.L. Wheeler, H.R. Dorfi, B.B Keum, Vibration modes of radial tires: measurement, prediction, and categorization under different boundary and operating conditions, *Proceedings of SAE Noise and Vibration Conference* 2005, Traverse City, USA, paper 2005-01-2523.
[28] E.J. Ni, D.S. Snyder, D.S. Walton, N.E. Mallard, G.E. Barron, J.T. Browell, B.N. Aljundi, Radiated noise from tire/wheel vibration, *Tire Science and Technology, TSTCA* 25 (1) (1997) 29–42.
[29] Z. Geng, A.A. Popov, D.J. Cole, Measurement, identification and modelling of damping in pneumatic tyres, *International Journal of Mechanical Sciences* 49 (2007) 1077–1094.
[30] R.S. Lakes, *Viscoelastic Solids*, first ed., CRC Press LLC, London, 1999.
[31] L. Garibaldi, H.N. Onah, *Viscoelastic Material Damping Technology*, Becchis Osiride, Torino, 1996.
[32] P. Kindt, F. De Coninck, P. Sas, W. Desmet, Experimental modal analysis of radial tires and the influence of tire modes on vehicle structure borne noise, *Proceedings of* 31*st FISITA* 2006 *World Automotive Congress*, Yokohama, Japan, 2006.
[33] L.R. Molisani, R.A. Burdisso, D. Tsihlas, A coupled tire structure/acoustic cavity model, *International Journal of Solids and Structures* 40 (2003) 5125–5138.
[34] E. Rustighi, S.J. Elliott, S. Finnveden, K. Gulyas, T. Mocsai, M. Danti, Linear stochastic evaluation of tyre vibration due to tyre/road excitation, *Journal of Sound and Vibration* 310 (2008) 1112–1127.
[35] R.J. Pinnington, Radial force transmission to the hub from an unloaded stationary tyre, *Journal of Sound and Vibration* 253 (5) (2002) 961–983.
[36] E. Stein, R. de Borst, T.J.R. Hughes, *Encyclopedia of Computational Mechanics, Solids and Structures*, Vol. 2, Wiley, England, 2004.
[37] D. Boulahbal, M. Muthukrishnan, Y. Shanshal, Tire mobility measurements: compensation for transducer and mounting effects, *Proceedings of SAE Noise and Vibration Conference* 2003, Traverse City, USA, paper 2003-01-1531.